Journal of Computational Physics 229 (2010) 5144–5160

Contents lists available at ScienceDirect

Journal of Computational Physics

journal homepage: www.elsevier.com/locate/jcp

A non-uniform basis order for the discontinuous Galerkin method of the 3D dissipative wave equation with perfectly matched layer

T. Lähivaara [a,*], T. Huttunen [a,b]

[a] Department of Physics and Mathematics, University of Eastern Finland, P.O. Box 1627, FI-70211 Kuopio, Finland
[b] Kuava Ltd., P.O. Box 1188, FI-70211 Kuopio, Finland

ARTICLE INFO

Article history:
Received 20 April 2009
Received in revised form 2 March 2010
Accepted 22 March 2010
Available online 30 March 2010

Keywords:
Discontinuous Galerkin
Wave propagation
Non-uniform basis order
Perfectly matched layer

ABSTRACT

In this study a discontinuous Galerkin method (DG) for solving the three-dimensional time-dependent dissipative wave equation is investigated. In the case of unbounded problems, the perfectly matching layer (PML) is used to truncate the computational domain. The aim of this work is to investigate a simple selection method for choosing the basis order for elements in the computational mesh in order to obtain a predetermined error level. The selection method studied here relies on the error estimates provided by Ainsworth [M. Ainsworth, Dispersive and dissipative behaviour of high order discontinuous Galerkin finite element methods, Journal of Computational Physics 198(1) (2004) 106–130]. The performance of the non-uniform basis is examined using numerical experiments. In the simulated model problems, a feasible method choosing the basis order for arbitrary sized elements is achieved. In simulations, the effect of dissipation and the choices of the PML parameters on the performance of the DG method are also investigated.

1. Introduction

Solving wave propagation in general geometries poses a significant challenge in scientific computation. During last decades several techniques have been explored to obtain a stable method that can efficiently approximate time-domain wave problems. Unfortunately, the widely used approaches, such as finite difference and finite element methods, suffer from numerical dispersion and dissipation which forces the use of dense spatial discretization and short time steps in the time integration. On the other hand, when the size of the computational domain increases, the density of the spatial discretization must increase to maintain a acceptable error level. This is commonly known as the numerical pollution [1,2].

The discontinuous Galerkin (DG) method has been proposed as a promising alternative for finite elements and finite difference methods for approximating large scale wave problems. Originally, in 1973 Reed and Hill applied the DG method to the steady-state Neutron transport equation [3]. After the original paper, the method has been extended to many fields of physics, including plasma physics [4,5], the Maxwell's equations and acoustic wave equations [6,7].

Here, we focus on the use of DG method to approximate unbounded acoustic wave problems. In these cases, the accuracy of the DG approximation can be affected several ways. These include:

1.1. Numerical flux

The DG method relies on the decomposition of the original wave problem into set of subproblems which are connected via an approximate numerical flux. The choice of the flux splitting method affects the accuracy [19]. In the present study, the flux proposed by Monk and Richter in [9] is used.

* Corresponding author.
E-mail address: timo.lahivaara@uef.fi (T. Lähivaara).

0021-9991/$ - see front matter © 2010 Elsevier Inc. All rights reserved.
doi:10.1016/j.jcp.2010.03.030

1.2. Time integration

There exists a large number of integration methods for time-dependent problems. These include the Runge–Kutta [7,24], space-time DG [9–11], ADER time integration methods using arbitrary high-order derivatives [12,14,13], and the Crank–Nicolson (CN) [23] scheme. In the current work, the low-storage Runge–Kutta (LSRK) time stepping scheme is used.

1.3. Polynomial basis order

The order of the polynomial basis can be chosen individually for each element in the computational mesh before and/or during the time integration (commonly referred to as *p*-adaptivity [13]). The choice of a basis order to achieve a tolerable level of accuracy is one of the main topics of this study.

1.4. Mesh density

The mesh size can be refined before and/or during the computation (known as *h*-adaptivity [15]). This topic is not investigated in this study.

1.5. Absorbing boundary condition

In many applications of physics and engineering, it is essential to replace the physical unbounded problem with an approximate problem in a bounded domain using a suitable absorbing boundary condition. In the current study, the perfectly matching layer (PML) is used.

In many cases the absorbing boundary condition (point 5) affects the accuracy of the solution, since unphysical reflections arise from the boundary. Numerous methods have been proposed to reduce the numerical reflections. For example, one promising solution for the problem is the arbitrarily high-order absorbing boundary condition (AHOC) proposed by Collino in [39]. The AHOC method is studied by Givoli in [31,32]. Another promising solution of reducing spurious reflections is the PML. Originally, the PML was proposed for the Maxwell's equations by Bérenger [25], but since then the method has been analyzed and extended to wide range of applications, see [26–30]. The PML is used also in this study to truncate the unbounded problem.

In this paper, our focus is to control the basis order (point 3) in the fixed mesh, instead of refining the mesh size. Originally, the selection method for the basis order was examined for the two-dimensional acoustic and elastic problems in Lähivaara and Huttunen [17]. In the current work, our aim is to extend this technique to the more realistic three-dimensional problems. We study only solutions of the acoustic wave equation. In this work, we consider the effect of wave dissipation and the PML parameters on the feasibility of the selection method. Theoretically the methods for choosing the optimal basis order is studied by Ainsworth [21] for the transport equation. Theoretical results shown in Ainsworth [21] are based on the dispersive and dissipate properties of the high-order DG methods. There also exists study of the dispersive and dissipative properties of the DG method for the second-order wave equation by Ainsworth et al. in [22]. Our approach relies on the theory provided by Ainsworth and collaborators but emphasis is on the numerical experiments using realistic model problems.

The numerical simulations are organized into two parts. First, a simple wave propagation in a homogeneous medium is examined using regularly refined tetrahedral meshes. First part begins with the study of the basic convergence analysis for the proposed numerical scheme. From these results, we obtain formulae that can be used to approximate the polynomial degrees of the basis for each element. These formulae give the basis order as a function of the local wave number and the element size. In the second part, the validity of the basis order selection method is tested using several numerical experiments using unstructured meshes. In these experiments, the effect of the PML and wave absorption for the accuracy of the method of choosing the basis degree are studied.

The structure of this article is as follows. First, in Section 2, we provide a short introduction to the equation governing dissipative wave propagation in three spatial dimensions. Furthermore, Section 2 introduces the discontinuous Galerkin method, the derivation of the unsplit PML, and finally a method for choosing the polynomial order of the basis functions. Section 3 is dedicated to the numerical experiments, and finally, in Section 4 draw conclusions from the results.

2. The lossy wave equation

This section presents the 3D dissipative wave equation in the form of a first-order hyperbolic system. Furthermore, the derivation of the DG method, unsplit PML for the wave equation, and finally, the theory for choosing the the basis order are presented.

Initial step is to define that Ω is a bounded Lipschitz domain in $\mathbb{R}^3$, $\boldsymbol{x} = (x_1, x_2, x_3) \in \Omega$ is the spatial variable, and $t \in [0, T]$ is time. Then, the linear dissipative acoustic wave equation can be written as

$$\frac{1}{c^2\rho}\frac{\partial^2 u}{\partial t^2} - \nabla \cdot \left(\frac{1}{\rho}\nabla u\right) + \beta\frac{\partial u}{\partial t} = 0 \quad \text{in } \Omega, \tag{1}$$

where u is the acoustic pressure, c is the wave speed, ρ is the density, and β is the absorption coefficient. In Eq. (1), the attenuation term $\beta\partial u/\partial t$ has been originally used for describing the attenuation of electromagnetic fields [37,34]. However, it has been shown that the attenuation model describes, for example, the dispersive attenuation of ultrasound in many soft tissues [37,38].

Next step is to write Eq. (1) in the form of a hyperbolic system [18]. For this purpose, a new vector $\boldsymbol{u}$ is defined as

$$\boldsymbol{u} = \begin{pmatrix} \boldsymbol{u}_1 \\ \boldsymbol{u}_2 \\ \boldsymbol{u}_3 \\ \boldsymbol{u}_4 \end{pmatrix} = \begin{pmatrix} \frac{\partial u}{\partial t} \\ \frac{1}{\rho}\frac{\partial u}{\partial x_1} \\ \frac{1}{\rho}\frac{\partial u}{\partial x_2} \\ \frac{1}{\rho}\frac{\partial u}{\partial x_3} \end{pmatrix}. \tag{2}$$

According to dissipative wave Eq. (1), the components of $\boldsymbol{u}$ satisfy the following equations

$$\frac{1}{c^2\rho}\frac{\partial \boldsymbol{u}_1}{\partial t} + \beta \boldsymbol{u}_1 - \nabla \cdot \begin{pmatrix} \boldsymbol{u}_2 \\ \boldsymbol{u}_3 \\ \boldsymbol{u}_4 \end{pmatrix} = 0, \tag{3}$$

$$\rho \frac{\partial}{\partial t}\begin{pmatrix} \boldsymbol{u}_2 \\ \boldsymbol{u}_3 \\ \boldsymbol{u}_4 \end{pmatrix} - \nabla \boldsymbol{u}_1 = 0. \tag{4}$$

Eqs. (3) and (4) can be expressed as a single linear hyperbolic system as follows

$$A\frac{\partial \boldsymbol{u}}{\partial t} + \sum_{j=1}^{3} A_j \frac{\partial \boldsymbol{u}}{\partial x_j} + B\boldsymbol{u} = 0, \tag{5}$$

where the matrices A and B are

$$A = \begin{pmatrix} \frac{1}{c^2\rho} & 0 & 0 & 0 \\ 0 & \rho & 0 & 0 \\ 0 & 0 & \rho & 0 \\ 0 & 0 & 0 & \rho \end{pmatrix}, \quad \text{and } B = \begin{pmatrix} \beta & 0 & 0 & 0 \\ 0 & 0 & 0 & 0 \\ 0 & 0 & 0 & 0 \\ 0 & 0 & 0 & 0 \end{pmatrix},$$

and where the matrices A_1, A_2, and A_3 for the spatial derivatives are

$$A_1 = \begin{pmatrix} 0 & -1 & 0 & 0 \\ -1 & 0 & 0 & 0 \\ 0 & 0 & 0 & 0 \\ 0 & 0 & 0 & 0 \end{pmatrix}, \quad A_2 = \begin{pmatrix} 0 & 0 & -1 & 0 \\ 0 & 0 & 0 & 0 \\ -1 & 0 & 0 & 0 \\ 0 & 0 & 0 & 0 \end{pmatrix}, \quad \text{and } A_3 = \begin{pmatrix} 0 & 0 & 0 & -1 \\ 0 & 0 & 0 & 0 \\ 0 & 0 & 0 & 0 \\ -1 & 0 & 0 & 0 \end{pmatrix}.$$

2.1. Initial and boundary conditions

For the unique solution of the hyperbolic system (5), initial and boundary conditions are needed. The initial condition can be written as

$$\boldsymbol{u} = \boldsymbol{u}_0 \quad \text{at } t = 0, \tag{6}$$

where the vector $\boldsymbol{u}_0$ contains the given initial values.

In this study, three boundary conditions for the boundary of the domain Ω are considered. These are the Neumann, Dirichlet, and impedance-type boundary conditions. All of these conditions can be expressed using the following formula

$$\sigma\frac{\partial u}{\partial t} + n \cdot \left(\frac{1}{\rho}\nabla u\right) = Q\left(-\sigma\frac{\partial u}{\partial t} + n \cdot \left(\frac{1}{\rho}\nabla u\right)\right) + \sqrt{2\sigma}g, \tag{7}$$

where n is a spatial outward unit normal, g is a source function, and σ is a real and positive parameter. With $Q = -1$, the inhomogeneous Neumann boundary condition is obtained in the form

$$n \cdot \left(\frac{1}{\rho}\nabla u\right) = \sqrt{\frac{\sigma}{2}}g. \tag{8}$$

On the other hand, the choice $Q = 1$ leads to the following condition

$$\frac{\partial u}{\partial t} = \frac{1}{\sqrt{2\sigma}}g, \tag{9}$$

which is known as the inhomogeneous Dirichlet boundary condition. Finally, the impedance-type boundary condition can be achieved by setting $Q = 0$. Then, Eq. (7) can be rewritten as follows

$$\sigma \frac{\partial u}{\partial t} + n \cdot \left(\frac{1}{\rho} \nabla u \right) = \sqrt{2\sigma} g. \tag{10}$$

When $\sigma = 1/c$, $Q = 0$, and the source term $g = 0$, the boundary condition (7) reduces to the lowest order Engquist–Majda absorbing boundary condition [33].

2.2. An unsplit version of the perfectly matching layer (PML)

In this section, the derivation of the PML for the hyperbolic system (5) is briefly outlined. The unsplit version of the PML is studied by Hu in Ref. [26].

Let us first transform the hyperbolic system (5) to the frequency-domain by setting $\partial/\partial t = -i\omega$ (ω is the angular frequency and i denotes imaginary unit), when we readily get

$$-i\omega A \tilde{\boldsymbol{u}} + \sum_{j=1}^{3} A_j \frac{\partial \tilde{\boldsymbol{u}}}{\partial x_j} + B \tilde{\boldsymbol{u}} = 0, \tag{11}$$

where $\tilde{\boldsymbol{u}}$ indicates the solution in the frequency-domain. Then, we introduce the partial differential operator (known as the complex stretching [41,28]) for the spatial terms as

$$\frac{\partial}{\partial x_j} \to \frac{\partial}{\partial x_j'} = \left(\frac{1}{1 + \frac{i d_{x_j}}{\omega}} \right) \frac{\partial}{\partial x_j}, \quad j = 1, \ldots, 3, \tag{12}$$

where $0 \leqslant d_{x_j}(\boldsymbol{x}) \in \mathbb{R}$, $j = 1, \ldots, 3$ (see Eq. (18)). Now, using Eq. (12) system (11) can be reformulated as

$$-i\omega A \tilde{\boldsymbol{u}} + \sum_{j=1}^{3} \left(\frac{1}{1 + \frac{i d_{x_j}}{\omega}} \right) A_j \frac{\partial \tilde{\boldsymbol{u}}}{\partial x_j} + B \tilde{\boldsymbol{u}} = 0. \tag{13}$$

Next step is to multiply Eq. (13) with $(1 + i d_{x_1}/\omega)(1 + i d_{x_2}/\omega)(1 + i d_{x_3}/\omega)$ to obtain

$$\begin{aligned}
(-i\omega A + B)\tilde{\boldsymbol{u}} &+ \sum_{j=1}^{3} \left\{ A_j \frac{\partial \tilde{\boldsymbol{u}}}{\partial x_j} + d_{x_j} A \tilde{\boldsymbol{u}} + \frac{i d_{x_j}}{\omega} B \tilde{\boldsymbol{u}} \right\} + \left\{ \frac{i(d_{x_2} + d_{x_3})}{\omega} - \frac{d_{x_2} d_{x_3}}{\omega^2} \right\} A_1 \frac{\partial \tilde{\boldsymbol{u}}}{\partial x_1} + \left\{ \frac{i(d_{x_1} + d_{x_3})}{\omega} - \frac{d_{x_1} d_{x_3}}{\omega^2} \right\} A_2 \frac{\partial \tilde{\boldsymbol{u}}}{\partial x_2} \\
&+ \left\{ \frac{i(d_{x_1} + d_{x_2})}{\omega} - \frac{d_{x_1} d_{x_2}}{\omega^2} \right\} A_3 \frac{\partial \tilde{\boldsymbol{u}}}{\partial x_3} + \frac{i(d_{x_1} d_{x_2} + d_{x_1} d_{x_3} + d_{x_2} d_{x_3})}{\omega} A \tilde{\boldsymbol{u}} - \frac{d_{x_1} d_{x_2} d_{x_3}}{\omega^2} A \tilde{\boldsymbol{u}} \\
&- \frac{(d_{x_1} d_{x_2} + d_{x_1} d_{x_3} + d_{x_2} d_{x_3})}{\omega^2} B \tilde{\boldsymbol{u}} - \frac{i d_{x_1} d_{x_2} d_{x_3}}{\omega^3} B \tilde{\boldsymbol{u}} = 0.
\end{aligned} \tag{14}$$

Eq. (14) can be transformed back to time-domain by introducing auxiliary variables $\boldsymbol{q}_1$, $\boldsymbol{q}_2$, and $\boldsymbol{q}_3$

$$\frac{\partial \boldsymbol{q}_1}{\partial t} = \boldsymbol{u}, \quad \frac{\partial \boldsymbol{q}_2}{\partial t} = \boldsymbol{q}_1, \quad \frac{\partial \boldsymbol{q}_3}{\partial t} = \boldsymbol{q}_2. \tag{15}$$

Thus, a reformulation using the unsplit physical variables is constructed as follows

$$A \frac{\partial \boldsymbol{u}}{\partial t} + \sum_{j=1}^{3} A_j \frac{\partial \boldsymbol{u}}{\partial x_j} + B \boldsymbol{u} + G = 0, \tag{16}$$

where

$$\begin{aligned}
G = &(d_{x_2} + d_{x_3}) A_1 \frac{\partial \boldsymbol{q}_1}{\partial x_1} + (d_{x_1} + d_{x_3}) A_2 \frac{\partial \boldsymbol{q}_1}{\partial x_2} + (d_{x_1} + d_{x_2}) A_3 \frac{\partial \boldsymbol{q}_1}{\partial x_3} + d_{x_2} d_{x_3} A_1 \frac{\partial \boldsymbol{q}_2}{\partial x_1} + d_{x_1} d_{x_3} A_2 \frac{\partial \boldsymbol{q}_2}{\partial x_2} + d_{x_1} d_{x_2} A_3 \frac{\partial \boldsymbol{q}_2}{\partial x_3} \\
&+ (d_{x_1} + d_{x_2} + d_{x_3}) A \boldsymbol{u} + (d_{x_1} d_{x_2} + d_{x_1} d_{x_3} + d_{x_2} d_{x_3}) A \boldsymbol{q}_1 + d_{x_1} d_{x_2} d_{x_3} A \boldsymbol{q}_2 + (d_{x_1} + d_{x_2} + d_{x_3}) B \boldsymbol{q}_1 \\
&+ (d_{x_1} d_{x_2} + d_{x_1} d_{x_3} + d_{x_2} d_{x_3}) B \boldsymbol{q}_2 + d_{x_1} d_{x_2} d_{x_3} B \boldsymbol{q}_3,
\end{aligned} \tag{17}$$

which is the form of the PML scheme used in this study. For simplicity, in the following we use the term G in equations when deriving the weak formulation for the DG scheme. One must note that term G is only required in the PML domain, elsewhere $G = 0$. Nevertheless, to simplify following discussion we do not distinguish PML and non-PML regions.

In the current study, the PML damping coefficients used in the computations are of the form

$$d_{x_\ell}(\boldsymbol{x}) = d_0 \left| \frac{x_\ell - x_0}{\vartheta} \right|^{\eta}, \quad \ell = 1, \ldots, 3, \tag{18}$$

where $0 \leqslant d_0 \in \mathbb{R}$ is parameter for the PML, x_0 denotes location, from which the numerical damping starts, ϑ is the PML thickness, and parameter η is the power for PML. The effect of parameters η, ϑ, and d_0 are simulated in Section 3.

2.3. The weak formulation

In this section, we outline the weak form of the DG method for the system of Eq. (5). For derivation details, we refer to the work by Monk and Richter [9].

For the DG method, the domain Ω is divided to N elements (in this work tetrahedra elements are used) so that

$$\Omega = \bigcup_{\ell=1}^{N} \Omega_\ell.$$

The boundary of the element Ω_ℓ is denoted by $\Gamma(\Omega_\ell)$.

To derive the weak form in the time-domain, the first step is to multiply Eq. (5) by a test function $\boldsymbol{v}^\top$ ($\top$ denotes the transpose) and integrate over the arbitrary element $\Omega_\ell \in \Omega$. This leads to a weak form which after the integration by parts can written as follows

$$a_K(\boldsymbol{u}, \boldsymbol{v}) = \int_{\Omega_\ell} \boldsymbol{v}^\top \left(A \frac{\partial \boldsymbol{u}}{\partial t} + \sum_{j=1}^{3} A_j \frac{\partial \boldsymbol{u}}{\partial x_j} + B\boldsymbol{u} + G \right) dV \tag{19}$$

$$= \int_{\Omega_\ell} \boldsymbol{v}^\top A \frac{\partial \boldsymbol{u}}{\partial t}\, dV - \sum_{j=1}^{3} \int_{\Omega_\ell} \frac{\partial \boldsymbol{v}^\top}{\partial x_j} A_j \boldsymbol{u}\, dV + \int_{\Omega_\ell} \boldsymbol{v}^\top (B\boldsymbol{u} + G)\, dV + \int_{\Gamma(\Omega_\ell)} \boldsymbol{v}^\top D \boldsymbol{u}\, dA = 0, \tag{20}$$

here the matrix D denotes the flux across $\Gamma(\Omega_\ell)$, ($\ell = 1 \ldots N$) in the direction of the normal n. The flux matrix D can be expressed as follows

$$D = \sum_{j=1}^{3} n_j A_j, \quad n = (n_1, n_2, n_3). \tag{21}$$

The matrix D can be split into a sum $D = D^+ + D^-$, where D^+ is positive semi-definite and D^- is negative semi-definite, and we assume that the matrix D can be also written as

$$D = \Xi(\Lambda^+ + \Lambda^-)\Xi^\top,$$

where Ξ is the orthogonal matrix containing the eigenvectors of D. The matrix Λ^+ contains the positive eigenvalues and the matrix Λ^- contains the negative eigenvalues. In general, D^+ is the "outflow boundary matrix" and D^- is the "inflow boundary matrix" [9]. We note that matrices D^+ and D^- satisfy important property

$$D^{\pm}(n) = D^{\mp}(-n).$$

Next, let $\Gamma_e(\Omega_\ell)$ denote an element boundary that coincides with the exterior boundary of the computational domain Ω. Furthermore, let $\Gamma_i(\Omega_\ell)$ be any interior element boundary within the domain Ω. To proceed in the derivation a suitable boundary condition for the element faces on the exterior boundary is needed. This can be written in the form

$$(D - \mathcal{N})\boldsymbol{u} = \boldsymbol{g} \quad \text{on } \Gamma, \tag{22}$$

where Γ is the boundary of the domain Ω, the matrix D is defined in Eq. (21), and the matrix $\mathcal{N}$ is defined later in this section (see Eq. (29)).

On interior element interfaces, a continuity condition must be enforced between two adjacent elements. Let $\widehat{\boldsymbol{u}}$ denote the field in a neighboring element of $\boldsymbol{u}$. Then, one can write the transmission condition for the interface between the two elements as follows

$$D^-\widehat{\boldsymbol{u}} = D^-\boldsymbol{u} \quad \text{on } \Gamma_i(\Omega_\ell). \tag{23}$$

By using the boundary condition (22) for element faces on the exterior boundary; and the transmission condition (23) and the matrix splitting $D = D^+ + D^-$ for the interior faces, the bilinear form for the element Ω_ℓ can be written as follows

$$a_K(\boldsymbol{u}, \boldsymbol{v}) = \int_{\Omega_\ell} \boldsymbol{v}^\top A \frac{\partial \boldsymbol{u}}{\partial t}\, dV - \sum_{j=1}^{3} \int_{\Omega_\ell} \frac{\partial \boldsymbol{v}^\top}{\partial x_j} A_j \boldsymbol{u}\, dV + \int_{\Omega_\ell} \boldsymbol{v}^\top (B\boldsymbol{u} + G)\, dV + \int_{\Gamma_i(\Omega_\ell)} \boldsymbol{v}^\top D^+ \boldsymbol{u}\, dA + \int_{\Gamma_i(\Omega_\ell)} \boldsymbol{v}^\top D^- \widehat{\boldsymbol{u}}\, dA$$

$$+ \int_{\Gamma_e(\Omega_\ell)} \boldsymbol{v}^\top (\mathcal{N}\boldsymbol{u} + \boldsymbol{g})\, dA. \tag{24}$$

Then using integration by parts again to Eq. (24), the following equation can be obtained

$$a_K(\boldsymbol{u},\boldsymbol{v}) = \int_{\Omega_\ell} \boldsymbol{v}^\top A \frac{\partial \boldsymbol{u}}{\partial t}\, dV + \sum_{j=1}^{3} \int_{\Omega_\ell} \frac{\partial \boldsymbol{v}^\top}{\partial x_j} A_j \boldsymbol{u}\, dV + \int_{\Omega_\ell} \boldsymbol{v}^\top (B\boldsymbol{u} + G)\, dV + \int_{\Gamma_i(\Omega_\ell)} \boldsymbol{v}^\top D^- (\widehat{\boldsymbol{u}} - \boldsymbol{u})\, dA - \int_{\Gamma_e(\Omega_\ell)} \boldsymbol{v}^\top (D - \mathcal{N})\boldsymbol{u}\, dA + \int_{\Gamma_e(\Omega_\ell)} \boldsymbol{v}^\top \boldsymbol{g}\, dA.$$

The right-hand side of the weak formulation, one gets the following equation for the field in a single element

$$a_K(\boldsymbol{u},\boldsymbol{v}) = 0. \tag{25}$$

Finally, if $\boldsymbol{u}_\ell$ denotes the field in the element Ω_ℓ, $\ell = 1,\ldots,N$ and $\boldsymbol{v}_\ell$ is the corresponding test function, the entire weak form is obtained via summation over all elements

$$\sum_{\ell=1}^{N} \left[\int_{\Omega_\ell} \boldsymbol{v}_\ell^\top \left(A \frac{\partial \boldsymbol{u}_\ell}{\partial t} + \sum_{j=1}^{3} A_j \frac{\partial \boldsymbol{u}_\ell}{\partial x_j} + B\boldsymbol{u}_\ell + G_\ell \right) dV + \sum_{k=1}^{N} \int_{\Gamma_i(\Omega_\ell)} \boldsymbol{v}_\ell^\top D^- (\boldsymbol{u}_k - \boldsymbol{u}_\ell)\, dA - \int_{\Gamma_e(\Omega_\ell)} \boldsymbol{v}_\ell^\top (D - \mathcal{N})\boldsymbol{u}_\ell\, dA \right] = -\sum_{\ell=1}^{N} \int_{\Gamma_e(\Omega_\ell)} \boldsymbol{v}_\ell^\top \boldsymbol{g}\, dA. \tag{26}$$

Note that the summation term over the neighboring elements (denoted by the subscript k) exists only if the elements Ω_ℓ and Ωk share a common interface so that $\Gamma_i(\Omega_\ell) \cap \Gamma_i(\Omega_k) \neq \varnothing$.

To discretize the weak formulation, the elementwise solutions $\boldsymbol{u}_\ell$, $\ell = 1,\ldots,N$ and the test functions $\boldsymbol{v}_\ell$ are approximated using the same polynomial basis functions. In the present study, the commonly used [20,7,19] Legendre polynomials are used as the basis functions.

2.4. Flux splitting

The flux splitting approach used in this paper was proposed by Monk and Richter [9]. There are numerous other techniques for flux splitting, such as the commonly used Lax–Friedrichs method, which was previously investigated in detail in Ref. [7].

To clarify the splitting of the matrix D, rewrite the matrix D of Eq. (21) as follows

$$D = \begin{pmatrix} 0 & -n_1 & -n_2 & -n_3 \\ -n_1 & 0 & 0 & 0 \\ -n_2 & 0 & 0 & 0 \\ -n_3 & 0 & 0 & 0 \end{pmatrix}. \tag{27}$$

Eigenvalues for D are $\lambda_1 = 1$, $\lambda_{2,3} = 0$, and $\lambda_4 = -1$. On the other hand, using the eigenvectors for the boundary matrix D (Eq. (27)), we have

$$D^+ = \frac{1}{2} \begin{pmatrix} -1 \\ n_1 \\ n_2 \\ n_3 \end{pmatrix} (-1, n_1, n_2, n_3), \quad D^- = -\frac{1}{2} \begin{pmatrix} 1 \\ n_1 \\ n_2 \\ n_3 \end{pmatrix} (1, n_1, n_2, n_3),$$

and then $D = D^+ + D^-$. To write more general boundary conditions, a new matrix must be defined. The matrix S can be written as follows

$$S = \begin{pmatrix} \sigma & 0 & 0 & 0 \\ 0 & 1 & 0 & 0 \\ 0 & 0 & 1 & 0 \\ 0 & 0 & 0 & 1 \end{pmatrix},$$

where parameter $0 < \sigma \in \mathbb{R}$. Since the choice of the parameter σ affects the accuracy of the approximation, our choice is based on the results shown in Lähivaara et al. [16]. The parameter σ is computed as

$$\sigma = \frac{2}{c^+ + c^-},$$

where c^+ and c^- are the wave speeds on the elements which share the common interface.

Then, using the definition of the matrix S, the boundary matrix D can be expressed in a more general form as follows

$$D = \frac{1}{\sigma} SDS \Longleftrightarrow D = \frac{1}{\sigma} SD^+S + \frac{1}{\sigma} SD^-S.$$

Now, matrices D_σ^+ and D_σ^- can be written in the following form

$$D_\sigma^+ = \frac{1}{2\sigma}\begin{pmatrix} -\sigma \\ n_1 \\ n_2 \\ n_3 \end{pmatrix}(-\sigma, n_1, n_2, n_3), \quad D_\sigma^- = -\frac{1}{2\sigma}\begin{pmatrix} \sigma \\ n_1 \\ n_2 \\ n_3 \end{pmatrix}(\sigma, n_1, n_2, n_3).$$

On the other hand, the matrices D_σ^+ and D_σ^- can be decomposed as

$$D_\sigma^+ = (\boldsymbol{l}^+)^\top \boldsymbol{l}^+, \quad D_\sigma^- = -(\boldsymbol{l}^-)^\top \boldsymbol{l}^-,$$

where column vectors $\boldsymbol{l}^{+,-}$ are defined as

$$\boldsymbol{l}^+ = \frac{1}{\sqrt{2\sigma}}(-\sigma, n_1, n_2, n_3), \quad \boldsymbol{l}^- = \frac{1}{\sqrt{2\sigma}}(\sigma, n_1, n_2, n_3).$$

The boundary condition (Eq. (7)) for the exterior boundary can be written in the following form using the definitions of $\boldsymbol{u}$ and the vectors $\boldsymbol{l}^-$ and $\boldsymbol{l}^+$

$$\boldsymbol{l}^- \boldsymbol{u} = Q\boldsymbol{l}^+ \boldsymbol{u} + g. \tag{28}$$

The next step is to multiply Eq. (28) with the term $(\boldsymbol{l}^-)^\top$, by which the following equation is obtained

$$(\boldsymbol{l}^-)^\top \boldsymbol{l}^- \boldsymbol{u} = Q(\boldsymbol{l}^-)^\top \boldsymbol{l}^+ \boldsymbol{u} + (\boldsymbol{l}^-)^\top g.$$

Hence, it is possible to choose the matrix $\mathcal{N}$ as follows

$$\mathcal{N} = D - 2(D_\sigma^- + Q(\boldsymbol{l}^-)^\top \boldsymbol{l}^+). \tag{29}$$

Rearranging terms in Eq. (29), the following form can be obtained

$$(D - \mathcal{N})\boldsymbol{u} = 2\left(D_\sigma^- + Q(\boldsymbol{l}^-)^\top \boldsymbol{l}^+\right)\boldsymbol{u} = -2(\boldsymbol{l}^-)^\top g. \tag{30}$$

Finally, the right-hand side of Eq. (22) can be written as

$$\boldsymbol{g} = -2(\boldsymbol{l}^-)^\top g, \tag{31}$$

where g is the source function defined in Eq. (7). Correspondingly, it is easy to derive the transmission condition (23) used on interior interfaces of the finite element mesh.

2.5. The choice of basis

In the present study, we focus on controlling the basis degree for an arbitrarily sized element instead of refining the mesh size. Ainsworth [21] has studied an optimal order estimate for the DG method from the theoretical point of view. Results shown in Ainsworth [21] predict that a super-exponential rate of convergence is obtained when

$$2p + 1 > kh + o(hk)^{1/3}, \tag{32}$$

where p is the order of the basis function, k is the wave number, h is the element size parameter, and o denotes the error function. The results of the study [21] indicate that the practical way to choose the degree of the basis functions for an arbitrary element is to set

$$2p + 1 \approx \kappa kh, \tag{33}$$

where κ is a free parameter (κ>1). In the next section, the validity of Eq. (33) is studied using 3D numerical experiments.

3. Numerical experiments

In the following three sections, we present the results of the numerical computations. In these experiments, our main goal is to study how to choose the basis order to obtain a relatively constant error level. In addition, we examined the effect of the Courant–Friedrichs–Lewy (CFL) number, perfectly matching layer (PML), and wave absorption for the accuracy of the basis degree selection method. In these examples the time derivative is approximated using the low-storage Runge–Kutta (LSRK) scheme.

The computer code used in this study is written in C++ and parallelized using the message passing interface (MPI). The mesh partitioning is handled using the Metis software [40]. The computations are done with 24 2.6 GHz Pentium 4 processors and having 96 GB total RAM; or Cray XT4/XT5 Massively Parallel Processor (MPP) supercomputer *Louhi*, which is part of the Finnish IT center for science (CSC) computing environment.

3.1. Wave propagation in a homogeneous medium

In this first example, wave propagation was studied in a homogeneous medium without using the PML. The domain for this example is a cube so that $\Omega = [-1, 1] \times [-1, 1] \times [-1, 1]$. The normalized material parameters for Eq. (1) were chosen so that wave speed $c = 1$, density $\rho = 1$. This example is separated in to three sections, from which in the first and second (Sections 3.1.1 and 3.1.2) the absorption coefficient $\beta = 0$. Initial condition $\widehat{\boldsymbol{u}}_0$ is equal to zero in this example. On the exterior boundary of the domain, an impedance-type boundary condition (7) with $Q = 0$ and $\sigma = 1/c$ was used.

The analytic solution for the model problem studied in Sections 3.1.1 and 3.1.2 can be written as

$$\boldsymbol{u} = \begin{pmatrix} g(ct - \boldsymbol{k}\cdot\boldsymbol{x}) \\ -\boldsymbol{k}_1 g(ct - \boldsymbol{k}\cdot\boldsymbol{x}) \\ -\boldsymbol{k}_2 g(ct - \boldsymbol{k}\cdot\boldsymbol{x}) \\ -\boldsymbol{k}_3 g(ct - \boldsymbol{k}\cdot\boldsymbol{x}) \end{pmatrix}, \tag{34}$$

where $\boldsymbol{k} = (1,0,0)$ and g is defined as (known as the mexican hat or Ricker wavelet)

$$g(s) = a_1\left(0.5 + a_2(s - t_0)^2\right)\exp\left(a_2(s - t_0)^2\right) \quad \forall s \geqslant 1, \tag{35}$$

where a_1 and t_0 are free parameters and $a_2 = -(\pi f)^2$ (f is the frequency). In this experiment the frequency f is equal to 2, parameter $a_1 = -1$, and $t_0 = 0.75$. In all model problems studied in following three sections, the time span was $t \in [0,2]$.

In this first experiment, the analytic and numerical solutions were compared at the final time instant in the whole computation domain Ω using the discrete L_2 error. The relative error is computed as follows

$$\sqrt{\frac{\sum_j \left(u_n(t_j) - u_e(t_j)\right)^2}{\sum_j \left(u_e(t_j)\right)^2}}, \tag{36}$$

where u_n is the numerical solution and u_e is the analytic solution. The relative error Eq. (36) was computed only for the component u_1 in all cases. In this paper, the relative error was examined as a function of the number of DOF, polynomial order p, and CFL number. The CFL number is

$$\mathrm{CFL} = \frac{\delta_t c}{h_{\min}}, \tag{37}$$

where δ_t is the length of the time step, c is the speed of sound, and $h_{\min}$ is the smallest distance between the two vertices in the element of the computational mesh.

3.1.1. Convergence analysis

The first part of this experiment is dedicated to the convergence analysis of the proposed numerical scheme. The goal is to verify that our code produces the known convergence behavior of the DG method (see [8,14]). For that purpose, wave propagation on regularly refined tetrahedral meshes is studied. Fig. 1 shows two meshes, which are used for the numerical convergence study.

Fig. 2 shows the relative error as a function of the CFL number and the mesh parameter $1/h_r$. The mesh parameter h_r is the maximum diameter of the circumscribed sphere of the tetrahedra. Results are computed with the constant polynomial order

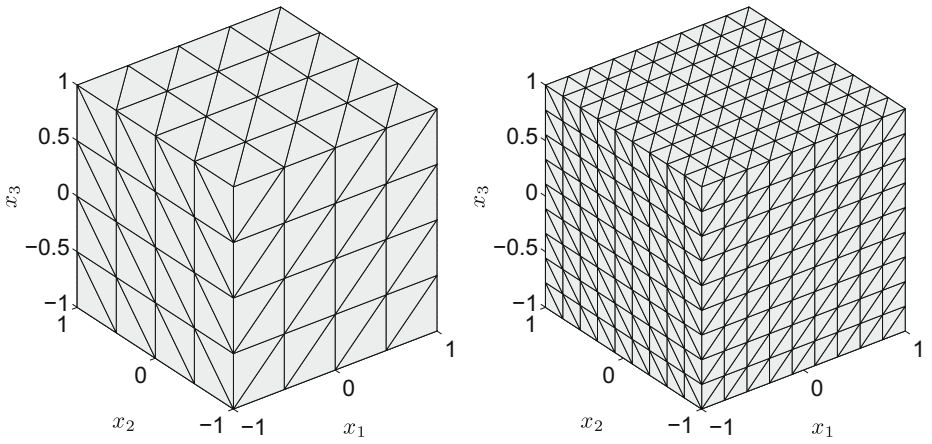

Fig. 1. Two discretizations of the computational domain Ω via regularly refined tetrahedral meshes.

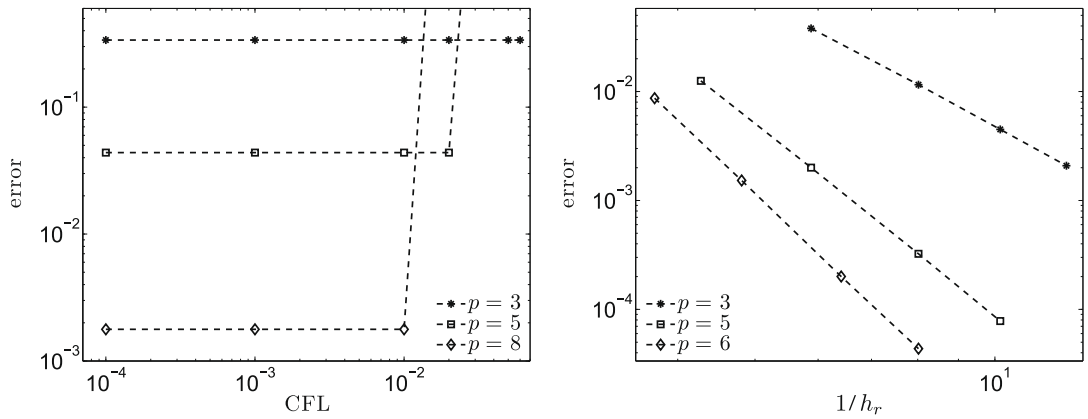

Fig. 2. (Left) The relative error as a function of the CFL number with the polynomial orders p = 3,5, and 8 in the mesh with 1296 elements and 343 vertices. (Right) The relative error as a function of the mesh parameter $1/h_r$ with the polynomial orders p = 3, 5, and 6.

in the each element. Obtained results confirm the known fact that the use of high-order basis with the DG method affects the limit of the CFL number. This subject is discussed in Ref. [8]. Based on these results, we use CFL number equal to 0.001 in all results shown in following sections. Results also confirm the fact that high-order convergence is achieved with the high-order DG schemes.

The numerical convergence order is for validating the chosen numerical schemes. The convergence order is be computed as

$$\mathcal{O}_{L^2} = \frac{\log_e(e^\ell) - \log_e(e^{\ell+1})}{\log_e\left(h_r^\ell\right) - \log_e\left(h_r^{\ell+1}\right)}, \tag{38}$$

where e^ℓ is the relative error obtained with the mesh ℓ. Table 1 shows the numerical convergence orders as a function of mesh parameter $1/h_r$ for three basis orders (results shown in Fig. 2). Results confirm that the optimal convergence orders ($\mathcal{O}_{L^2} \approx p + 1$) are achieved with the high-order DG method evaluated with the LSRK time stepping scheme.

3.1.2. A non-uniform basis order

In the second part of this example, our aim is to find equations which can be used for approximating the degree of the basis functions for each element of the computational mesh. The idea of the order selection is to obtain a relatively constant error level from the solution. For this purpose we plot the polynomial order p as a function of the parameter kh for three levels of the relative error (10%, 1%, and 0.1%). Results are computed in the regularly refined tetrahedral meshes (Fig. 1).

For the computed results, we seek a relationship of the form

$$p = akh + b, \tag{39}$$

where p is the order of the polynomial basis functions, k is the wave number, and h is the mesh parameter. The mesh parameter is chosen

Table 1
The numerical convergence order $\mathcal{O}_{L^2}$ as a function of the mesh parameter h_r for three p-orders (3 (upper), 5 (middle), and 6 (lower)). In table, all reported relative error values are multiplied with factor 10^2.

h_r	Error	$\mathcal{O}_{L^2}$
0.1701	3.7966	–
0.1247	1.1558	3.8346
0.0985	0.4490	4.0000
0.0813	0.2085	4.0143
0.2339	1.2524	–
0.1701	0.2004	5.7547
0.1247	0.0324	5.8777
0.0985	0.0078	6.0113
0.2673	0.8690	–
0.2079	0.1526	6.9222
0.1559	0.0200	7.0551
0.1247	0.0044	6.8340

$$h = \frac{1}{4}\sum_{\ell=1}^{4} \left| \boldsymbol{x}_{CM}^{K} - \boldsymbol{x}_{\ell}^{K} \right|, \tag{40}$$

where $\boldsymbol{x}_{CM}^{K}$ is the position of the centroid of arbitrary tetrahedron K and $\boldsymbol{x}_{\ell}^{K}, \ell = 1,\ldots,4$ are the coordinates of the vertices. In Eq. (39), a and b are the parameters to be solved. One must note that Eq. (39) is comparable to the optimal order estimate provided by Ainsworth (Eq. (33)). Parameters a and b solved by least squares data fitting.

Fig. 3 shows fitted curves, computed results, and the demanded error level as a function of the slope of the fitted line. The data into which the fitting is applied are chosen so that they are the maximum kh for each polynomial order p. Results obtained from the data fitting are reported in Table 2. Table 2 shows the slope a and the axis-intercept b of the fitted line (also the error levels) for the each stipulated error level. Results (Table 2 and Fig. 3) predict that the parameter b does not dominate the obtained polynomial order.

To test the proposed basis order selection method in practice, the wave propagation is evaluated in non-uniform meshes. Fig. 4 shows an example of the non-uniform meshes used in computations. Figure shows also the number of elements as a

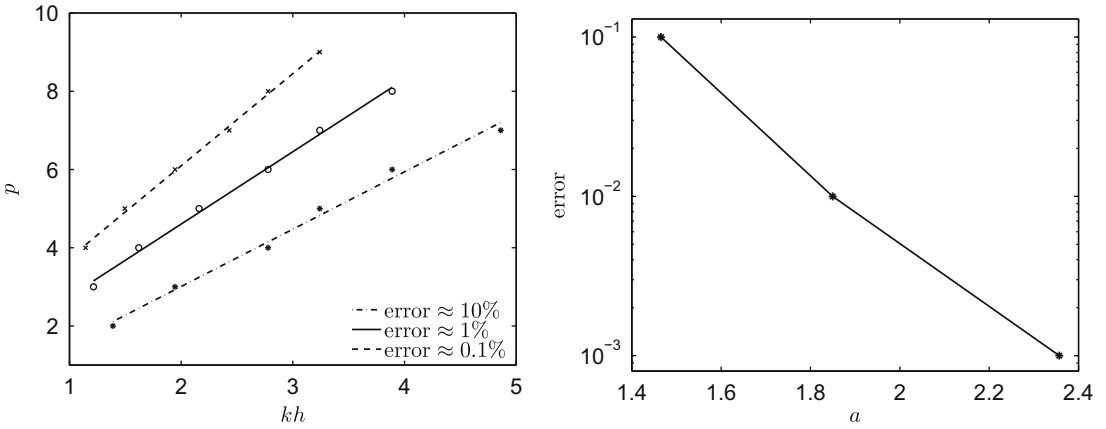

Fig. 3. (Left) The polynomial order p as a function of the parameter kh for three error levels with the CFL number equal to 0.001. (Right) The stipulated error level as a function of the parameter a (the slope of the line). Parameters a and b are shown in Table 2.

Table 2
Parameters $a \pm \Delta a$ and $b \pm \Delta b$ obtained using least squares data fitting.

	Error ≈ 10%	Error ≈ 1%	Error ≈ 0.1%
a	1.4655	1.8498	2.3569
Δa	0.0705	0.0562	0.0516
b	0.0775	0.9040	1.3788
Δb	0.2279	0.1489	0.1183

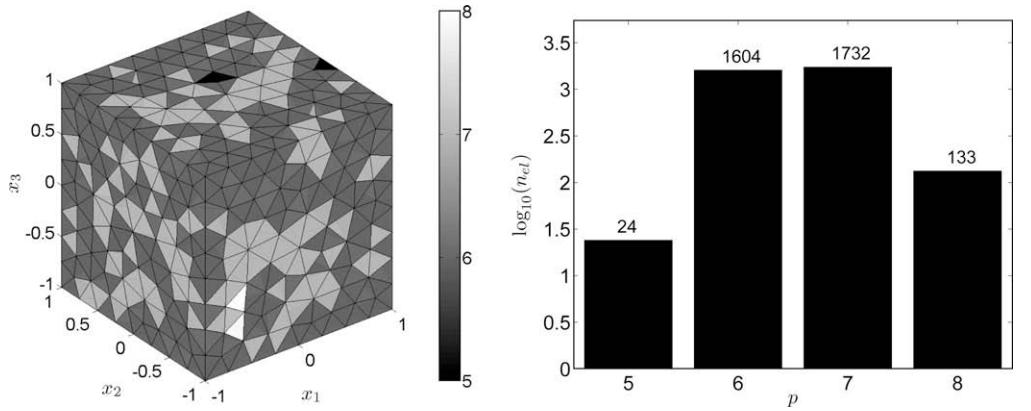

Fig. 4. (Left) An example mesh with 3493 elements and 827 vertices. (Right) The number of the elements n_{el} as a function of the polynomial degree p. The distribution of the order of the basis function is obtained with error level 0.1%.

function of the polynomial order for the visualized mesh. The mesh consists of 3493 elements and 827 vertices (see Table 3 for more details). The polynomial basis order distribution is obtained with 0.1% demanded relative error level.

Fig. 5 shows the relative error as a function of the number of the DOF. In this experiment basis orders for each element are chosen using fitted curves (see Table 2 for details). Details of the meshes used in the computations are shown in Table 3. The table reports the number of elements, the number of vertices, and the shortest and longest distance between two vertices in the computational mesh ($h_{\min}$ and $h_{\max}$). Results predict that obtained error levels are near the requested values.

3.1.3. Attenuation of the plane wave

The final part of this first experiment is dedicated to study the effect of the absorption parameter β for the accuracy of the basis order selection method. For the impedance-type boundary condition the continuous plane wave source is used. The source function defined as

$$g(t) = \sin(\omega t) \quad \forall t, \tag{41}$$

where $\omega = 4\pi$.

Analytic solution for the term $\boldsymbol{u}_1$ is computed using the Fourier-transform. First we apply the Fourier-transform to the wave source shown in Eq. (41). Then, the solution in the frequency-domain is solved individually for each frequency component. Finally, the analytic solution in the time-domain is obtained using the inverse Fourier-transform. Analytic solutions for the lossy wave equations are widely studied, these include [34–36].

Fig. 6 shows the relative error as a function of the absorption coefficient β in the mesh with 16,394 elements and 3345 vertices and the relative error as a function of the number of the DOF with $\beta = 2/3$. Our results show that there does not exist notable effect with the fixed absorption coefficient $\beta = 2/3$ for the relative error level when choosing the basis order as shown in Table 2. On the other hand, when the mesh is fixed and β is varied the choice of p fails to keep the demanded relative error level. Here the demanded relative error level was 1.0%. The details of the meshes used in this experiment are reported in Table 3.

3.2. The effect of the PML

In this second example, wave propagation was studied in a homogeneous medium with the PML. The domain for this example is a cube so that $\Omega = [-0.5-\vartheta, 0.5+\vartheta] \times [-0.5-\vartheta, 0.5+\vartheta] \times [-0.5-\vartheta, 0.5+\vartheta]$, where ϑ denotes the PML thickness. In this case, the normalized material parameters for the dissipative wave Eq. (1) were chosen so that wave speed $c = 1$, density $\rho = 1$, and absorption parameter $\beta = 0$. On the exterior boundary of the domain, an absorbing boundary condition (7) with $Q = 0$, $g = 0$, and $\sigma = 1/c$ was used. The simulation time is chosen so that $t \in [0, 3]$.

In this experiment, the sound source is generated using an initial condition (6)

Table 3
Meshes used in the simulation. The table lists the number of elements and the number of vertices for each mesh. In addition, $h_{\min}$ is the shortest and $h_{\max}$ is the longest distance between two vertices in the mesh.

	Mesh 1	Mesh 2	Mesh 3	Mesh 4	Mesh 5
Elements	2320	3493	4894	7253	16394
Vertices	582	827	1119	1579	3345
$h_{\min}$	0.1930	0.1700	0.1427	0.1275	0.0859
$h_{\max}$	0.5337	0.4559	0.4146	0.3550	0.2753

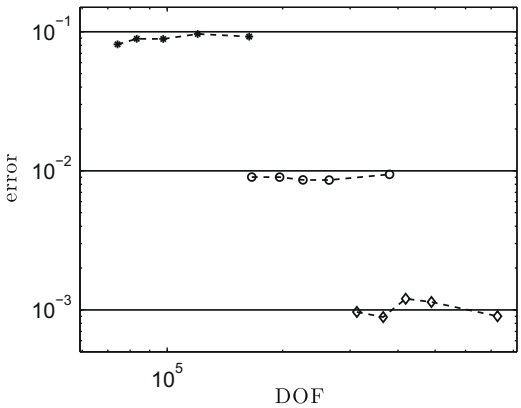

Fig. 5. The relative error as a function of the number of the DOF with the CFL number equal to 0.001. Solid lines shows the stipulated error levels.

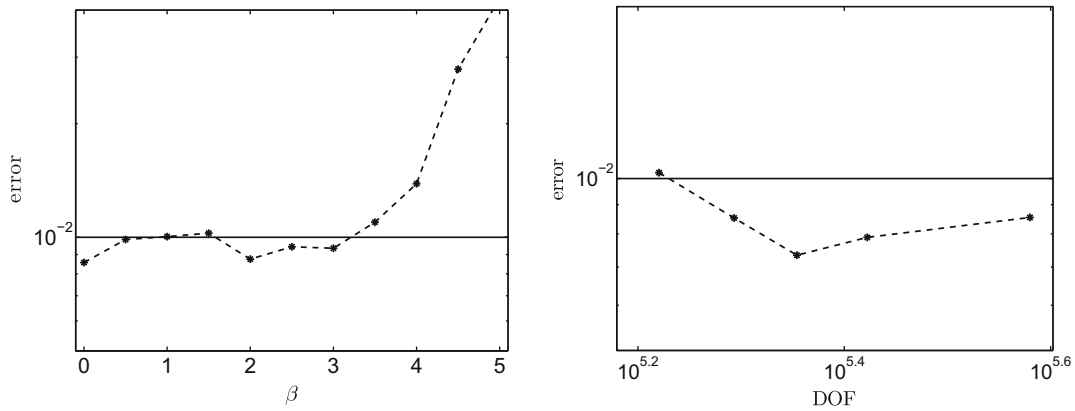

Fig. 6. (Left) The relative error as a function of absorption coefficient β in the mesh with 16,394 elements and 3345 vertices. (Right) The relative error as a function of the number of the DOF with the absorption parameter $\beta = 2/3$. Solid line shows the 1.0% error level.

$$\boldsymbol{u}_0 = \begin{pmatrix} \exp\left(-\alpha \sum_{\ell=1}^{3} (x_\ell - x_0)^2\right) \\ 0 \\ 0 \\ 0 \end{pmatrix},$$

where $\alpha = 40$ and $x_0 = 0.15$. The "exact" solution is computed in domain $\Omega = [-4, 4] \times [-4, 4] \times [-4, 4]$ with a constant polynomial order ($p = 7$) in each element. The used computational mesh consists of 56,130 elements and 10,771 vertices ($h_{\max} = 0.3946$ and $h_{\min} = 0.1023$).

Fig. 7 shows an example mesh used in simulations. Visualized mesh consists of 10,015 elements and 2124 vertices (see Table 4 for more details). Figure shows also the basis order distribution which is obtained using (39) with the demanded relative error level 1.0%.

Fig. 8 shows the relative error as a function of the power η in the mesh consisting of 5646 elements and 1242. In results we also simulate the relative error as a function of the parameter d_0 using three values for the PML thickness ($\vartheta = 0.2$, 0.3, and 0.4). In this experiment the relative error is computed at the spatial position $(-0.4,-0.4,-0.4)$ as a function of time for all cases. Results predict that it is reasonable to set power η equal to 2 in despite the PML thickness. Results show also that if the PML thickness ϑ is increased, the value for the parameter d_0 can be chosen more freely. For example, if we choose $\vartheta = 0.2$ the value for d_0 must be [30, 60] but if we take $\vartheta = 0.4$ the suitable value for $d_0 \in [20, 90]$.

3.3. Loudspeaker

In this final experiment, the aim is study wave propagation in the more realistic model problem. Here, the bass element of the loudspeaker is used as a sound source and propagation of the emitted wave is studied in an unbounded domain. Moti-

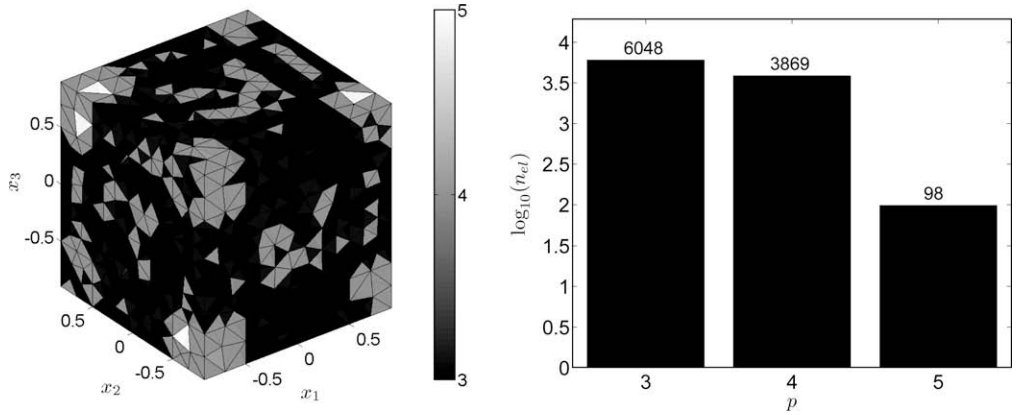

Fig. 7. (Left) An example mesh used in computations including 10,015 elements and 2124 vertices. Right: The number of the elements n_{el} as a function of the polynomial order p. The demanded error level was equal to 1.0%.

Table 4
Computation meshes used in the example. The table shows the number of elements and the number of vertices for each mesh. Here, $h_{\min}$ is the shortest and $h_{\max}$ is the longest distance between two vertices in the mesh and ϑ is the PML thickness.

	Mesh 1	Mesh 2	Mesh 3
Elements	5646	7922	10015
Vertices	1242	1717	2124
$h_{\min}$	0.1000	0.0963	0.0858
$h_{\max}$	0.3464	0.2942	0.3422
ϑ	0.2	0.3	0.4

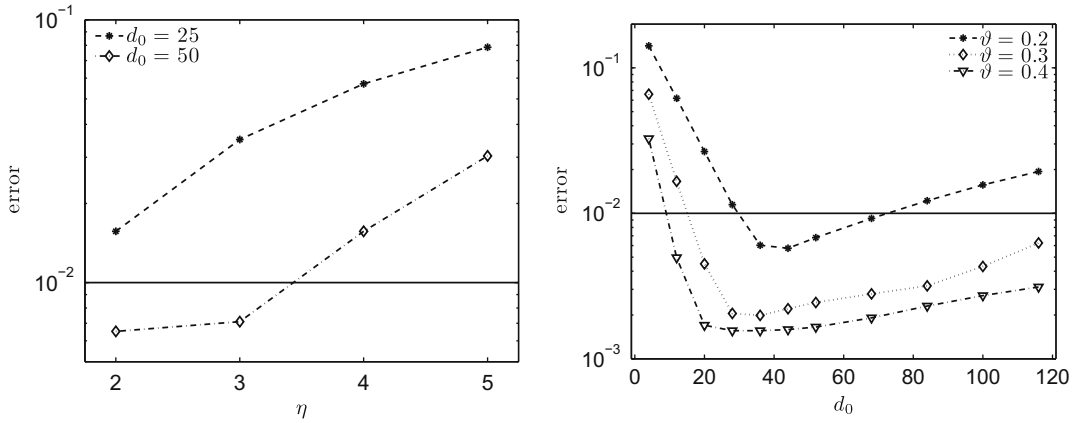

Fig. 8. (Left) The relative error as a function of power η for two values of d_0 (CFL = 0.001 and ϑ = 0.2). (Right) The relative error as a function of parameter d_0 for three PML thickness values (ϑ = 0.2, 0.3, and 0.4) with η = 2. Solid line denotes the demanded 1.0% error level.

vation for this experiment is to investigate the non-uniform basis (Section 3.1.2) and, on the other hand, the choices for the PML parameter (Section 3.2).

The problem domain is $\Omega = [-0.17-\vartheta, 0.17+\vartheta]$ m $\times [-0.2125-\vartheta, 0.2125+\vartheta]$ m $\times [-0.83-\vartheta, 0.83+\vartheta]$ m, where the PML thickness ϑ = 0.25 m and dimensionless parameter d_0 = 50. The power parameter η is equal to 2 in this model example. The problem geometry (Fig. 9) consists of a loudspeaker and the surrounding free space. The material parameters for Eq. (1) are

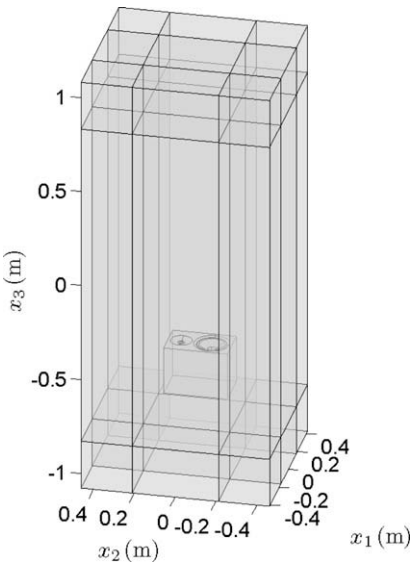

Fig. 9. The geometry for the model problem.

as the speed of sound $c = 343$ m/s, density $\rho = 1.2$ kg/m^3, and absorption coefficient $\beta = 0$. On the exterior boundary the absorbing boundary condition ($Q = 0$, $\sigma = 1/c$, and $g = 0$) is used. Initial condition $\boldsymbol{u}_0 = 0$ in this model problem.

In this example, the sound is introduced using the inhomogeneous Neumann boundary condition ($Q = -1$) on the bass surface of the loudspeaker (see Fig. 10 for more details). The sound source for the simulations is written as follows

$$g(t) = \exp\left(-\alpha(t - t_0)^2\right) \sin\left(\omega(t - t_0)\right) \forall t, \tag{42}$$

where $\alpha = 90$, $t_0 = 0.87$ ms and $\omega = 2\pi f$ (frequency $f = 1400$ Hz). In simulation the time t spans from 0 to 8.75 (ms). Other parts of the loudspeaker are modeled with the homogeneous Neumann boundary condition ($Q = -1$ and $g = 0$).

Fig. 10 shows the cross section of the whole computation mesh, surface mesh of the loudspeaker, and the number of elements as a function of the polynomial order. The mesh used in computations consists of 35,828 elements and 6969 vertices ($h_{\min} = 0.45$ cm and $h_{\max} = 0.1546$ m). In this experiment, the stipulated relative error level was equal to 0.1%. The surface mesh shows that we use more denser mesh in the front surface since it contains more geometric details.

Fig. 11 shows the pressure amplitude as a function of the time. The pressure field is visualized at the spatial position $(0, 0, 0.5)$ m. Result shows that there does not exist any reflections from the external boundary but, on the other hand, from the figure can be seen the reflection which arises from the tweeter element.

Fig. 12 demonstrates snapshots of the pressure field at times $t = 1.52$ ms, 2.71 ms, and 4.84 ms. As in the previous experiment, also in this case the pressure field is only visualized inside the non-PML region. The snapshots were chosen so that at the first time instant ($t = 1.52$ ms) the speaker still emits the wave. In the second time instant $t = 2.71$ ms the sound is completely generated from the bass surface of the loudspeaker. On the other hand, at the second time instant, from the results show the reflection which arises from the tweeter element. In the final time instant ($t = 4.84$ ms) the wave is propagated at the end of the non-PML region.

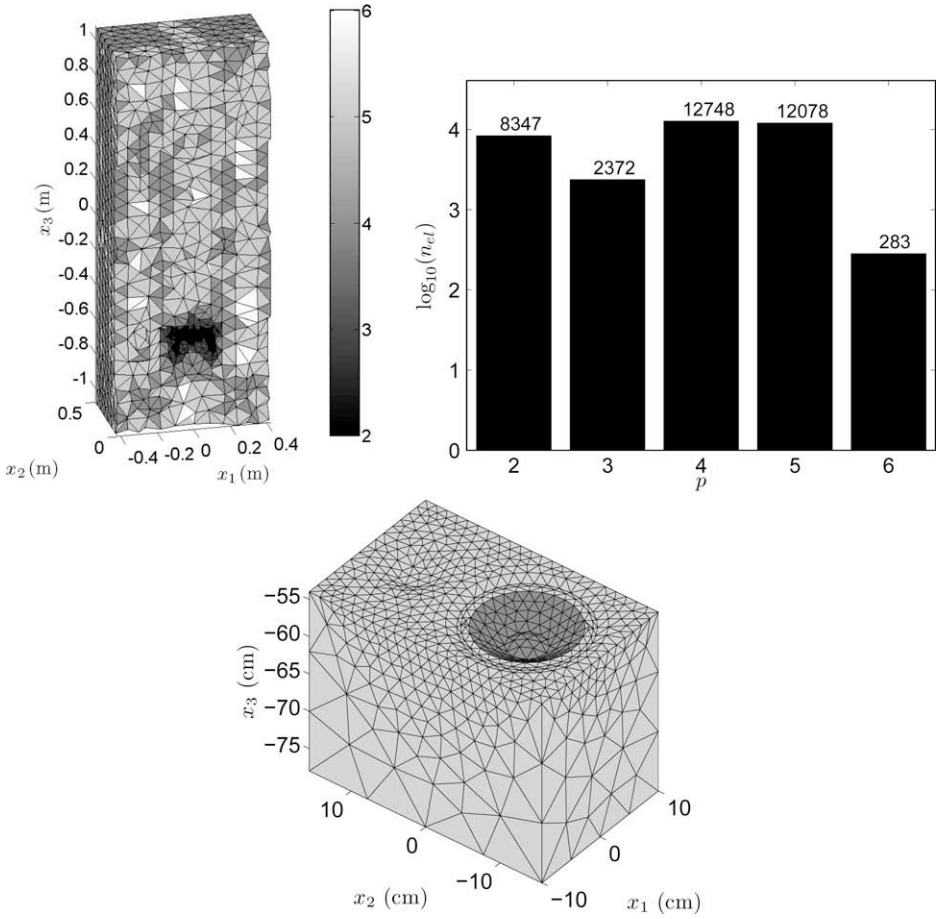

Fig. 10. (TopLeft) A cross section mesh with 35,828 elements and 6969 vertices ($h_{\min} = 0.45$ cm and $h_{\max} = 0.1546$ m). (TopRight) The number of elements as a function of the polynomial degree. (Bottom) The surface mesh of the loudspeaker. The sound source is shown with different color in the surface mesh. The distribution obtained with the stipulated error level equal to 0.1%.

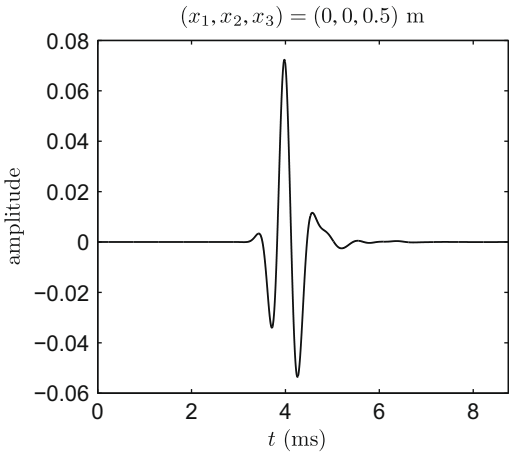

Fig. 11. The pressure amplitude as a function of the time at the spatial position (0,0,0.5) m.

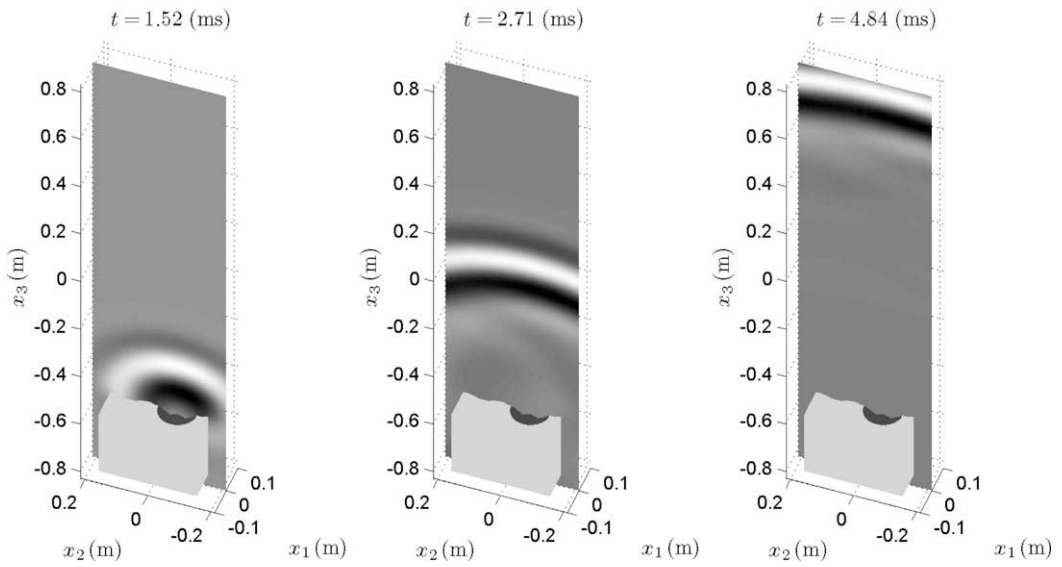

Fig. 12. The snapshots of the pressure fields. Solutions are computed in a mesh with 35,828 elements and 6969 vertices. The title shows the time point of the pressure field. The surface of the loudspeaker is included in the each snapshot.

4. Conclusions

In this paper, the DG method for solving the 3D dissipative wave equation with the unsplit PML was examined. The main purpose of the paper was to study how to choose the order of the polynomial basis functions for the elements in the computational mesh to obtain a predetermined error level. For this purpose, wave propagation was studied in homogeneous domain using regularly refined tetrahedral meshes. Next, the data fitting was evaluated to obtain equations for the selection method of the basis order. In simulations, the system of choosing the degree of the basis was tested using different numerical experiments.

In simulations, the effect of the wave dissipation for the accuracy of the selection method was evaluated. In the experiments we simulated the performance of the PML for truncating the unbounded problem. For the PML we evaluated several parameters which have great influence to the accuracy of the solution. We observed that appropriate selection of the parameters related to the PML is needed in order to obtain a acceptable accuracy of the solution.

Results suggest that it is possible to obtain a selection method for the basis order so that a relatively constant error level is achieved. In this system of choosing the basis order, the polynomial degree can be chosen for each the element before starting time integration and it does not change during the integration. Hence, this system saves the computational capacity and overall time needed to reach a requested accuracy of the approximation.

Results shown in Table 2 indicates that the parameter b does not have major influence to the basis degree obtained using the selection method. However, for the demanded error level 0.1% parameter $b \approx 1.4$ increases easily the obtained p-order with 1. This roughly means that the polynomial order is always at least 2 when the demanded error level is 0.1%. This is misleading since, one can assume that, if the mesh is dense enough the error level 0.1% is achieved with $p = 1$. However, one can also assume that if the demanded error level is obtained with $p = 1$ it is also obtained with $p = 2$. Same conclusion was also made in the 2D simulations [17] the parameter was $b < 1.5$). On the other hand, when comparing values for the slope of the fitted curve we find that parameters a for 2D simulations are comparable to 3D ones with factor approximately 2. This phenomena can be explained with the different type of choices for the mesh parameter h.

Finally, we want to point out that the basis parameters of this study are obtained only for the acoustic wave problems (see Section 2). The accuracy of DG method may be different for other types wave problems and DG formulations. It is clear that, the method will fail in the case of singular wave fields and/or non-smooth sources functions [17] in which a suitable hp-adaptive method is needed. A model problem of the failure is shown in Lähivaara and Huttunen [17]. Hence, it may be necessary to re-tune the optimal basis parameters by using the proposed basis selection method and a suitable reference solution.

Acknowledgments

The authors wish to thank the Finnish IT Center for Science (CSC), the Cultural Foundation of Northern Savo, and the Emil Aaltonen foundation for financial support.

References

[1] G.C. Cohen, Higher-Order Numerical Methods for Transient Wave Equations, Springer-Verlag, 2002.
[2] F. Ihlenburg, Finite Element Analysis of Acoustic Scattering, Springer, 1998.
[3] W. Reed, T. Hill, Triangular Mesh Methods for the Neutron Transport Equation, Technical Report LA-UR-73-479, Los Alamos National Laboratory, Los Alamos, New Mexico, USA, 1973.
[4] J. Loverich, U. Shumlak, A discontinuous Galerkin method for the full two-fluid plasma model, Computer Physics Communications 169 (1-3) (2005) 251–255.
[5] G. Lin, G.E. Karniadakis, A discontinuous Galerkin method for two-temperature plasmas, Computer Methods in Applied Mechanics and Engineering 195 (25–28) (2006) 3504–3527.
[6] B. Riviére, M. Wheeler, Discontinuous finite element methods for acoustic and elastic wave problems, Contemporary Mathematics (2003).
[7] J.S. Hesthaven, T. Warburton, Nodal high-order methods on unstructured grids I. Time-domain solution of Maxwell's equations, Journal of Computational Physics 181 (1) (2002) 186–221.
[8] J.S. Hesthaven, T. Warburton, Nodal Discontinuous Galerkin Methods; Algorithms, Analysis, and Applications, Springer, 2007.
[9] P. Monk, G.R. Richter, A discontinuous Galerkin method for linear symmetric hyperbolic systems in inhomogeneous media, Journal of Scientific Computing 22–23 (1) (2005) 443–477.
[10] C.M. Klaij, J.J.W. van der Vegt, H. van der Ven, Space-time discontinuous Galerkin method for the compressible Navier–Stokes equations, Journal of Computational Physics 217 (2) (2006) 589–611.
[11] O. Karakashian, C. Makridakis, A space-time finite element method for the nonlinear Schrödinger equation: the discontinuous Galerkin method, Mathematics of Computation 67 (222) (1998) 479–499.
[12] M. Käser, M. Dumbser, An arbitrary high-order discontinuous Galerkin method for elastic waves on unstructured meshes I: the two-dimensional isotropic case with external source terms, Geophysical Journal International 166 (23) (2006) 855–877.
[13] M. Dumbser, M. Käser, E.F. Toro, An arbitrary high-order discontinuous Galerkin method for elastic waves on unstructured meshes V: local time stepping and p-adaptivity, Geophysical Journal International 171 (2) (2007) 695–717.
[14] M. Dumbser, M. Käser, E.F. Toro, An arbitrary high-order discontinuous Galerkin method for elastic waves on unstructured meshes II: the three-dimensional study, Geophysical Journal International 167 (1) (2000) 319–336.
[15] P.-E. Bernard, N. Chevaugeon, V. Legat, E. Deleersnijder, J.-F. Remacle, High-order h-adaptive discontinuous Galerkin methods for ocean modelling, Ocean Dynamics 57 (2) (2007) 109–121.
[16] T. Lähivaara, M. Malinen, J.P. Kaipio, T. Huttunen, Computational aspects of the discontinuous Galerkin method for the wave equation, Journal of Computational Acoustics 16 (4) (2008) 507–530.
[17] T. Lähivaara, T. Huttunen, A non-uniform basis order for the discontinuous Galerkin method of the acoustic and elastic wave equations, Applied Numerical Mathematics, submitted for publication.
[18] K. Friedrichs, Symmetric positive linear differential equations, Communications on Pure and Applied Mathematics 11 (1) (1958) 333–418.
[19] F.Q. Hu, M.Y. Hussaini, R. Rasetarinera, An analysis of the discontinuous Galerkin method for wave propagation problems, Journal of Computational Physics 151 (2) (1999) 921–946.
[20] M. Dubiner, Spectral methods on triangles and other domains, Journal of Scientific Computing 6 (4) (1991) 345–390.
[21] M. Ainsworth, Dispersive and dissipative behaviour of high order discontinuous Galerkin finite element methods, Journal of Computational Physics 198 (1) (2004) 106–130.
[22] M. Ainsworth, P. Monk, W. Muniz, Dispersive and dissipative properties of the discontinuous Galerkin finite element methods for second-order wave equation, Journal of Scientific Computing 27 (1–3) (2006) 5–40.
[23] A. Quarteroni, R. Sacco, F. Saleri, Numerical Mathematics, Springer, 2000.
[24] M.H. Carpenter, C.A. Kennedy, Fourth-order 2 N-storage Runge–Kutta Schemes, NASA-TM-109112, 1994.
[25] J.-P. Bérenger, A perfectly matched layer for the absorption of electromagnetic waves, Journal of Computational Physics 114 (2) (1994) 185–200.
[26] F.Q. Hu, A stable, perfectly matched layer for linearized Euler equations in unsplit physical variables, Journal of Computational Physics 173 (2) (2001) 455–480.
[27] J. Diaz, P. Joly, A time domain analysis of PML models in acoustics, Computer Methods in Applied Mechanics and Engineering 195 (2) (2006) 3820–3853.
[28] F. Collino, P. Monk, Optimizing the perfectly matched layer, Computer Methods in Applied Mechanics and Engineering 164 (1) (1998) 157–171.
[29] E. Bécache, P.G. Petropoulos, S.D. Gedney, On the long-time behavior of unsplit perfectly matched layers, IEEE Transactions on Antennas and Propagation 52 (5) (2004) 1335–1342.
[30] S. Abarbanel, D. Gottlieb, J.S. Hesthaven, Well-posed perfectly matched layers for advective acoustics, Journal of Computational Physics 154 (2) (1999) 266–283.
[31] D. Givoli, High-order non-reflecting boundary conditions without high-order derivatives, Journal of Computational Physics 170 (2) (2001) 849–870.

[32] D. Givoli, B. Neta, High-order non-reflecting boundary scheme for time-dependent waves, Journal of Computational Physics 186 (1) (2003) 24–46.
[33] B. Engquist, A. Majda, Absorbing boundary conditions for the numerical simulation of waves, Mathematics of Computation 31 (1) (1977) 629–651.
[34] T. Szabo, Causal theories and data for acoustic attenuation obeying a frequency power law, The Journal of the Acoustical Society of America 97 (1) (1995) 14–24.
[35] T. Szabo, Time domain wave equations for lossy media obeying a frequency power law, The Journal of the Acoustical Society of America 96 (1) (1994) 491–500.
[36] R.S.C. Cobbold, N.V. Sushilov, A.C. Weathermon, Transient propagation in media with classical or power-law loss, The Journal of the Acoustical Society of America 116 (6) (2004) 3294–3303.
[37] S. Leeman, L. Hutchins, J.P. Jones, Bounded pulse propagation, Acoustical Imaging 10 (1982) 427–435.
[38] S. Leeman, L. Hutchins, J.P. Jones, Pulse scattering in dispersive media, Acoustical Imaging 11 (1982) 139–147.
[39] F. Collino, High order absorbing boundary conditions for wave propagation models: straight line boundary and corner cases, in: R. Kleinman (Ed.), Proceedings of the Second International Conference on Mathematical and Numerical Aspects of Wave Propagation, SIAM, Delaware, 1993, pp. 161–171.
[40] G. Karypis, V. Kumar, A fast and high quality multilevel scheme for partitioning irregular graphs, SIAM Journal on Scientific Computing 20 (1) (1998) 359–392.
[41] W.C. Chew, W.H. Weedon, A 3D perfectly matched medium from modified Maxwell's equations with stretched coordinates, Microwave and Optical Technology Letters 7 (13) (1994) 599–604.